



# Topography of epithelial–mesenchymal plasticity

Francesc Font-Clos<sup>a</sup>, Stefano Zapperi<sup>a,b</sup>, and Caterina A. M. La Porta<sup>c,1</sup>

<sup>a</sup>Center for Complexity and Biosystems, Department of Physics, University of Milan, 20133 Milano, Italy; <sup>b</sup>Consiglio Nazionale delle Ricerche, Istituto di Chimica della Materia Condensata e di Tecnologie per l'Energia, 20125 Milano, Italy; and <sup>c</sup>Center for Complexity and Biosystems, Department of Environmental Science and Policy, University of Milan, 20133 Milano, Italy

Edited by José N. Onuchic, Rice University, Houston, TX, and approved April 27, 2018 (received for review December 29, 2017)

**The transition between epithelial and mesenchymal states has fundamental importance for embryonic development, stem cell reprogramming, and cancer progression. Here, we construct a topographic map underlying epithelial–mesenchymal transitions using a combination of numerical simulations of a Boolean network model and the analysis of bulk and single-cell gene expression data. The map reveals a multitude of metastable hybrid phenotypic states, separating stable epithelial and mesenchymal states, and is reminiscent of the free energy measured in glassy materials and disordered solids. Our work not only elucidates the nature of hybrid mesenchymal/epithelial states but also provides a general strategy to construct a topographic representation of phenotypic plasticity from gene expression data using statistical physics methods.**

epithelial–mesenchymal transition | epigenetic landscape | Boolean networks

**E**pithelial (E) cells can transdifferentiate into mesenchymal (M) cells and vice versa under a cohort of transcription factors, including the Snail and Zeb families (1). The E to M transition (EMT), associated with the loss of cell–cell adhesion and the gain of invasive traits, is considered to be a hallmark of plasticity within a stem cell population and is particularly relevant for tumors. For this reason, a great effort has been devoted in the past to identify the critical biological functions regulating the EMT and its reverse, the M to E transition (MET). Almost 80% of human malignancies originate from E tissues, and a transition toward an M phenotype is usually associated with more aggressive potential (2–5). Emerging evidence shows that the EMT is a multiple-step process where cells express a mix of markers, both characteristic of E and M cells (6–8). These recent results are blurring the rigid distinction between E and M phenotypes, indicating that cancer cells can acquire hybrid E/M phenotypes, combining invasive capabilities with intracellular adhesion (9, 10), becoming extremely aggressive and associated with poor patient outcome (11, 12).

According to an old and influential metaphor from Waddington (13), the cell phenotype is analogous to a marble rolling over an epigenetic landscape, and phenotypic plasticity corresponds to the marble crossing a hill separating different valleys. This landscape should correspond to the attractors of the kinetics of gene regulatory networks (14–21) and be encoded in gene expression data (22, 23). Here, we combine numerical simulations of a large Boolean model for the EMT–MET network with the analysis of a wide set of bulk and single-cell gene expression data to reconstruct the topography underlying E/M plasticity. Genetic circuits regulating the EMT have been widely investigated theoretically, with models ranging from simple switches composed of a few genes (24) to large complex networks requiring extensive numerical simulations, in both discrete (25, 26) and continuous time (27). Some of these models have provided insights into particular EMTs, generating hypotheses that have later been experimentally tested (26). We show how these models can be used to rationalize and classify genetic drivers of the EMT and clarify the nature of hybrid E/M states guided by the Waddington picture (13).

Our results reveal that EMT/MET occurs across an extremely complex landscape characterized by a startling number of valleys and mountains organized according to a scale-free hierarchical statistical pattern. We observe a multitude of stable E/M

states separated by a series of progressively less stable and more hybrid states that are increasingly prone to phenotypic changes in response to external perturbations. Hence, EMTs and METs can take place in widely different locations and across multiple paths, in close analogy with nonequilibrium phase transitions in disordered solids (28, 29).

## Model

To reconstruct the topographic landscape of E/M plasticity, we chose to build on the large Boolean network model previously used to investigate EMT in hepatocellular carcinoma (25, 26). Since the model as it stands is hardwired toward EMT and MET is completely suppressed, we added to the model a missing contribution from the LIF/KLF4 pathway, whose role for MET has been widely reported (30, 31) (see *SI Appendix*, Fig. S1, Dataset S1, and *SI Appendix* for details). In this way, we obtained a network of  $N = 72$  nodes, whose state is defined by a string of binary variables  $\{s_i\}$ , determining if each gene/factor  $i$  is expressed/present ( $s_i = 1$ ) or not ( $s_i = -1$ ). Regulatory relations between two nodes  $i$  and  $j$  were encoded into a (nonsymmetric) matrix  $J_{ij}$  taking the value  $J_{ij} = 1$  if  $j$  promotes  $i$  and  $J_{ij} = -1$  when  $j$  inhibits  $i$  (see Dataset S2). The network nodes evolve asynchronously according to a simple majority rule, so that the node is set to  $s_i = 1$  if the sum of its promoting interactions is larger than the sum of its inhibitory ones (see Fig. 1A) (32). In case of ties, the node was not updated, keeping its present state (15). This evolution rule is the binary version of the half-functional rule recently proposed in ref. 27 to construct continuum kinetic reaction models from pathways and can be formally expressed as

$$s_i(t+1) = \text{sign} \left( \sum_j J_{ij} s_j(t) \right), \quad [1]$$

## Significance

**Cells can change their phenotype from epithelial to mesenchymal during development and in cancer progression, where this transition is often associated with metastasis and poor disease prognosis. Here we show this process involves the transit through a multitude of metastable hybrid phenotypes in a way that is similar to the driven dynamics of disordered materials. Our method shows that highly aggressive hybrid epithelial/mesenchymal cell phenotypes are located in metastable regions that can easily switch under external and internal perturbations. We propose a general mapping strategy that can be used for other pathways, providing a useful tool to visualize the ever increasing number of gene expression data obtained from single cells and tissues.**

Author contributions: S.Z. and C.A.M.L.P. designed research; F.F.-C. performed research; F.F.-C. analyzed data; and F.F.-C., S.Z., and C.A.M.L.P. wrote the paper.

The authors declare no conflict of interest.

This article is a PNAS Direct Submission.

Published under the PNAS license.

<sup>1</sup>To whom correspondence should be addressed. Email: caterina.laporta@unimi.it.

This article contains supporting information online at [www.pnas.org/lookup/suppl/doi:10.1073/pnas.1722609115/-DCSupplemental](http://www.pnas.org/lookup/suppl/doi:10.1073/pnas.1722609115/-DCSupplemental).

Published online May 21, 2018.

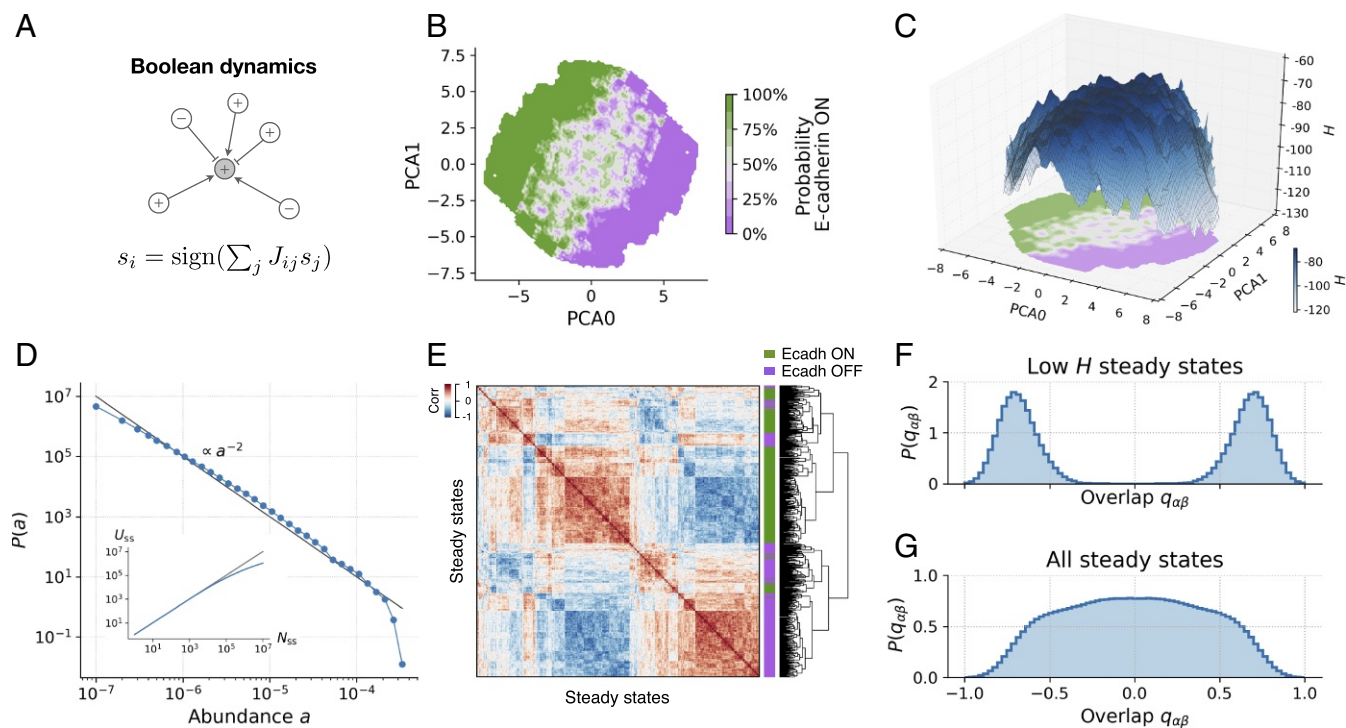


**Fig. 1.** The topography of E/M states displays a hierarchical complex structure. (A) Illustration of the Boolean update rule. The state of a node  $s_i$  depends on the state of its promoters ( $J_{ij} = +1, \rightarrow$ ) and inhibitors ( $J_{ij} = -1, \leftarrow$ ). (B) PCA projection of  $10^6$  steady states. Color corresponds to the ratio of steady states that express E-cadherin. The panel shows intricate patterns of transition between areas of high/low Ecadherin expression probability, colored in green/violet shades. (C) A 3D reconstruction of topography of EMT. The  $xy$  projection reproduces the data in B. The  $z$  axis corresponds to the value of  $H$ , showing that high- $H$  states (colored in darker blue shades) coincide with the central transition area in B. (D) Distribution of steady-state abundances, computed from  $10^7$  steady states of the EMT model (blue symbols). The relative abundance  $a$  of a steady state is the fraction of times it is found, starting from random initial conditions. The black line of slope  $-2$  is shown only as a guide to the eye. The *Inset* shows the number of distinct steady states  $U_{ss}$  as a function of the total number of steady states  $N_{ss}$  found in the simulations. (E) Clustering of steady states, computed using 500 steady states of the model. The heat map shows the correlation between steady states. Colors adjacent to the dendrogram mark the expression of E-cadherin (green) or lack of expression (violet). States expressing E-cadherin cluster together but display additional hierarchical organization. (F) Overlap distribution over the 20% of steady states with lowest  $H$ . A two-peak distribution marks the presence of two symmetric sets as in disordered magnets. (G) The broad overlap distribution over all steady states resembles the one observed in spin glasses.

which is the same equation used to simulate the zero-temperature dynamics in random ferromagnets (28) and spin glasses (29). (Modifications of the model that include local random fields and their relation to network reconstruction errors are discussed in *SI Appendix*. See also *SI Appendix, Fig. S8*.) Guided by the analogy with magnetic systems, we defined a pseudo-Hamiltonian  $H = -\sum_{i,j} J_{ij} s_i s_j$ . When interactions are strictly symmetric ( $J_{ij} = J_{ji}$ ), the fixed points of Eq. 1 are local minima of  $H$ . This is not guaranteed in our case since the interaction matrix is not symmetric (33, 34). We can, however, still show that  $H$  is lowered under repeated application of the evolution rule in Eq. 1 (see *SI Appendix* for full derivations and *SI Appendix, Fig. S9*). Hence,  $H$  provides a measure of the stability of a network state, with low- $H$  states being more stable than high- $H$  states.

**Results**

**Simulated E/M Topography Displays Fractal Features.** A phenotypic landscape associated with our EMT/MET network can be reconstructed by performing a large number ( $M_0 = 10^7$ ) of simulations, starting from random initial conditions until the network reaches a steady state where  $s_i$  does not change. (No limit cycles are found; see *SI Appendix* for details.) In this way, we find a large number of distinct steady states that can be projected into a two-dimensional map using principal component analysis (PCA). We classify these steady states according to the expression of E-cadherin (CDH1), which we use as a reporter of the E/M phenotype (see Fig. 1B). The E/M map reconstructed from the model shows a clear separation between E and M states, with a

boundary layer where E and M states coexist in very close proximity. A topographic representation of the stability of the states can be obtained by projecting  $H$  on the same two-dimensional map (Fig. 1C) showing that the boundary layer is more elevated with respect to pure E/M states, suggesting that those states are less stable. Furthermore, the map displays a very rough topography, with two main valleys separated by a large barrier populated by smaller and smaller valleys.

Given the sheer amount of distinct steady states (see Fig. 1D, *Inset*), we resorted to a statistical analysis and computed the probability distribution  $P(a)$  of the relative abundances of the states, where  $a$  is the fraction of times we find a given state. Fig. 1D shows that  $P(a)$  is a power law distribution, indicating that most of the states are very rarely found [when  $a$  is small,  $P(a)$  is large], but few states are found multiple times [when  $a$  is large,  $P(a)$  is small]. Alternative functional forms for  $P(a)$  are discussed in *SI Appendix* and shown in *SI Appendix, Fig. S10*. The presence of a power law is a signature of a scale-free fractal organization of the states, as is also apparent by the correlation matrix of the states. Fig 1E shows the presence of large correlated clusters subdivided into smaller and smaller clusters. In the physics of disordered systems, a hierarchical organization of the states is traditionally revealed by a broad distribution  $P(q_{\alpha\beta})$  of states' overlap  $q_{\alpha\beta} = \sum_i (s_i^\alpha s_i^\beta) / N$ , measuring the similarity between two states  $\{s_i^\alpha\}$  and  $\{s_i^\beta\}$  (35). Hierarchical ground state structures have been observed in short-range Ising spin glasses (see refs. 36 and 37). When we restrict the sampling to low- $H$  states,  $P(q_{\alpha\beta})$  displays a two-peak structure, indicating the presence of

two classes of distinct and separate states (Fig. 1*F*), but when we consider all steady states, the overlap distribution becomes very broad, resembling the one observed in spin glasses, as noticed a long time ago for random Boolean networks (38–40).

**Simulated Phenotypic Transitions Reveal Scale-Free Stochastic Fluctuations.** Once the topography associated with the E/M landscape has been established, we investigate how the landscape changes when each one of the nodes is held fixed to  $s_i = \pm 1$ , which simulates overexpression (OE) or knockdown (KD) of the corresponding gene (see *SI Appendix* for details). As an example, Fig. 2*A* and *B* reports the one-dimensional projection of the topography under OE or KD of the SNAIL1 gene, a well-known inducer of the EMT. SNAIL1 OE leads to a rightward tilt of the landscape, favoring the M phenotype, while under SNAIL1 KD, the landscape tilts to the left, favoring the E state. This behavior is reminiscent of the effect of a magnetic field in a disordered magnet, where the free-energy landscape tilts in the direction of the field. If the network is initially in an E state, SNAIL1 OE can induce EMT, but the success rate and the trajectory crucially depend on the initial state (see Fig. 2*C*), with high- $H$  states much more likely to undergo EMT than low- $H$  states (see *SI Appendix*, Fig. S2). The variability in the outcome resulting from the OE/KD of a single gene can also be quantified by measuring the distribution of the number of nodes  $z$  affected by the process (see Fig. 2*D*). The distribution decays as power law  $P(z) \sim z^{-\tau}$ , up to a cutoff value that increases with the  $H$  value of the initial state (see Fig. 2*E*), a further indication that high- $H$  states are more susceptible to fluctuations (see also *SI Appendix*, Fig. S2). The avalanche exponent of the power law distribution is  $\tau \approx 3/2$ , a value expected for mean-field avalanches in driven disordered systems (28).

Using the model, it is possible to perform OE/KD on all of the nodes and estimate the probability of each node to induce EMT or MET (see Fig. 2*F*). Ranking the nodes as a function of

their relevance for EMT, we recover well-known EMT inducers such as SNAIL1, ZEB1, or TGF- $\beta$  and MET suppressors such as KLF4 and mir-200. The general pattern is that an inducer of EMT by OE also induces MET by KD and similarly for MET. We also simulate a transient version of OE/KD where a node is switched ( $s_i \rightarrow -s_i$ ), but it is then allowed to eventually relax back to its previous state. The results summarized in *SI Appendix*, Fig. S2 are similar to those obtained under stable OE/KD, for which the node variable is held fixed throughout the simulation, but the probability of EMT/MET is always smaller.

**E/M Topography Inferred from Gene Expression Data Agrees with Simulations.** To confirm that the topographic representation of the E/M landscape obtained through the model provides an accurate representation of cellular phenotype, we examined the large cohort of gene expression data from human tissues provided by the GTEx project (41). To directly compare experimental data to the model, we designed a simple binarization strategy to decide whether a gene is expressed or not in a particular sample or cell. To calibrate the binarization scale, we used skin cells and fibroblasts as reference E and M states, respectively, and set a threshold based on the expression distribution of each gene in these two datasets (see Fig. 3*A* and *SI Appendix*). Genes whose expression was above the threshold were assigned to  $s_i = 1$  and otherwise to  $s_i = -1$ . The same threshold could then be used to binarize all of the 11,688 transcriptomes from different tissues present in the GTEx database.

Using the topographic map of the E/M landscape constructed from simulations, we could then localize individual samples projecting their gene expression data on the map as shown in Fig. 3*B*. We then used the model to infer the stability of each phenotype by computing  $H$  associated to each state (Fig. 3*C*). When we plotted skin cells and fibroblasts on a two-dimensional map, we saw that they correctly fell into E or M regions, respectively (see Fig. 3*B*), but not all samples had the same value of  $H$  (see

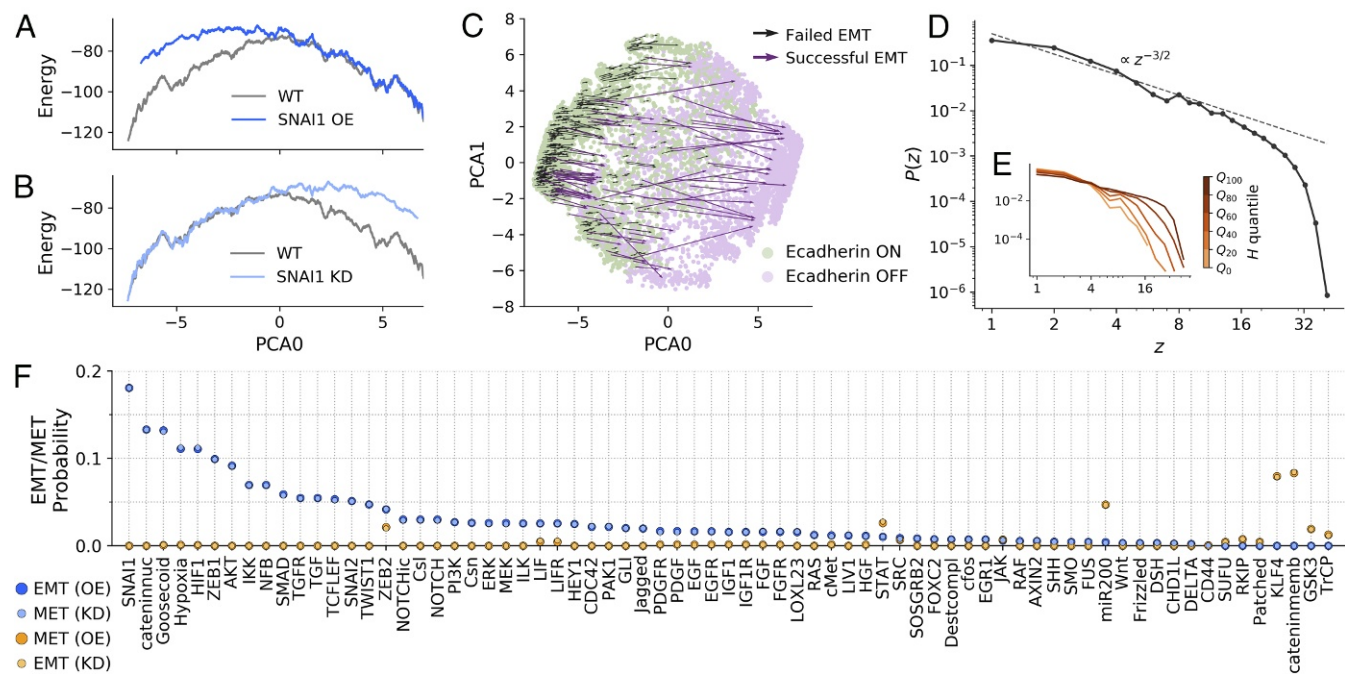


**Fig. 2.** EMT/MET occurs with different probabilities through multiple paths. The model shows many forms of EMT/MET, and these occur with different probabilities. (A and B) One-dimensional PCA projection of the  $H$  landscape where (A) OE or (B) KD of SNAIL1 tilts the landscape toward the M or E regions, respectively. (C) Transition map under SNAIL1 OE. The model displays different forms of SNAIL1-induced EMT. (D) The distribution of gene expression avalanches after individual KD/OE is a power law with exponent  $\tau \approx 1.5$ . (E) The cutoff of the distribution depends on  $H$ , quantified here by quartiles, with high- $H$  states producing larger avalanches. (F) EMT/MET probabilities under KD/OE conditions. The model lays out a nondeterministic picture of EMT/MET, where well-known factors such as SNAIL1 (EMT) or KLF4 (MET) induce phenotypic transitions with higher probability (see *Materials and Methods* and *SI Appendix*, Fig. S2 for further details).







when the reference samples were of unequal size. The statistical significance of the binarization procedure was assessed with the Fisher's exact test. The EMT–MET model takes into account the localization of  $\beta$ -catenin by considering two separate nodes: one for  $\beta$ -catenin located in the nucleus, and one for  $\beta$ -catenin in the membrane. In gene-expression datasets, it is not possible to infer the localization of  $\beta$ -catenin looking only at the expression level of CTNNB1. To circumvent this issue, we considered  $\beta$ -catenin to be in the nucleus if its targets TCF/LEF were expressed, and in the membrane otherwise. If CTNNB1 was not expressed, the state of both nodes was set to  $-1$  independently of the value of TCF/LEF.

**Datasets.** Data in Fig. 3 came from the GTEx project (41) and were downloaded from the GTEx portal (<https://gtexportal.org/home/datasets>) on October 12, 2017. We used samples labeled as “Cells–Transformed Fibroblasts” and “Skin–Not Sun Exposed (Suprapubic)” as reference samples for binarization. The PCA basis presented in Fig. 3 B and C was computed using all GTEx samples. All nodes were included in this analysis. The TGF- $\beta$ -induced EMT data presented in Fig. 4A were downloaded from the Gene Expression Omnibus (accession no. GSE17708) (42) on September 25, 2017. We used  $T = 0.5$ , 1 h and  $T = 24$ , 72 h as reference samples for binarization. A total of 29 nodes with a binarization  $P$  value below 0.05 were included in the analysis. We used  $10^7$  steady states from the model, restricted to such nodes, to compute the PCA basis in Fig. 4A. Dox-induced MET data in Fig. 4B were downloaded from the Gene Expression Omnibus (accession no. GSE21757) (30), on October 2, 2017. We used  $T = 0$  d and  $T = 21$  d as

reference samples for binarization. With one single sample per time point, binarization  $P$  values could not be computed as explained above. As an alternative, we restricted the analysis to 47 nodes with a fold-change greater than or equal to 0.5. We used  $10^7$  steady states from the model, restricted to such nodes, to compute the PCA basis in Fig. 4B. Single-cell data of embryonic-to-endoderm differentiation presented in Fig. 4C were downloaded from the Gene Expression Omnibus (accession no. GSE75748) (43), on September 25, 2017. We used  $T = 0$  h and  $T = 96$  h as reference samples. Given the large number of samples, the PCA basis presented in Fig. 4C was computed using the experimental data. All nodes were included in the analysis. Head and neck cancer single-cell data presented in Fig. 4 D and E were obtained from the Gene Expression Omnibus (accession no. GSE103322). We used E and fibroblast samples as reference samples for binarization. The PCA basis was fitted to the single-cell data using all nodes. The pEMT score was computed as the average expression of the 100 genes that constitute the pEMT program in ref. 45. Fibroblast-to-cardiomyocyte differentiation data in *SI Appendix, Fig. S6* were downloaded from the Gene Expression Omnibus [accession nos. GSE98570 (bulk data) and GSE98567 (single-cell data)] (44), on November 22, 2017. We used samples labeled as “control” and “reprogramming cells” as reference samples for single-cell data binarization and samples labeled as “D0” and “D14” for bulk data binarization. Single-cell data were used to fit the PCA basis presented in *SI Appendix, Fig. S7*.

**ACKNOWLEDGMENTS.** F.F.-C. and S.Z. are supported by European Research Council Advanced Grant 291002 SIZEEFFECTS.

- Ye X, Weinberg RA (2015) Epithelial-mesenchymal plasticity: A central regulator of cancer progression. *Trends Cell Biol* 25:675–686.
- Huber MA, Kraut N, Beug H (2005) Molecular requirements for epithelial-mesenchymal transition during tumor progression. *Curr Opin Cell Biol* 17:548–558.
- Rhim AD, et al. (2012) EMT and dissemination precede pancreatic tumor formation. *Cell* 148:349–361.
- Sarrió D, et al. (2008) Epithelial-mesenchymal transition in breast cancer relates to the basal-like phenotype. *Cancer Res* 68:989–997.
- Aleskandarany MA, et al. (2014) Epithelial mesenchymal transition in early invasive breast cancer: An immunohistochemical and reverse phase protein array study. *Breast Cancer Res Treat* 145:339–348.
- Bitterman P, Chun B, Kurman RJ (1990) The significance of epithelial differentiation in mixed mesodermal tumors of the uterus. A clinicopathologic and immunohistochemical study. *Am J Surg Pathol* 14:317–328.
- Haraguchi S, Fukuda Y, Sugisaki Y, Yamanaka N (1999) Pulmonary carcinosarcoma: Immunohistochemical and ultrastructural studies. *Pathol Int* 49:903–908.
- Paniz Mondolfi AE, et al. (2013) Primary cutaneous carcinosarcoma: Insights into its clonal origin and mutational pattern expression analysis through next-generation sequencing. *Hum Pathol* 44:2853–2860.
- Revenu C, Gilmour D (2009) Emt 2.0: Shaping epithelia through collective migration. *Curr Opin Genet Dev* 19:338–342.
- Yu M, et al. (2013) Circulating breast tumor cells exhibit dynamic changes in epithelial and mesenchymal composition. *Science* 339:580–584.
- Jolly MK, et al. (2016) Stability of the hybrid epithelial/mesenchymal phenotype. *Oncotarget* 7:27067–27084.
- George JT, Jolly MK, Xu S, Somarelli JA, Levine H (2017) Survival outcomes in cancer patients predicted by a partial EMT gene expression scoring metric. *Cancer Res* 77:6415–6428.
- Waddington C (1957) *The Strategy of the Genes* (Allen & Unwin, London).
- Kauffman SA (1969) Metabolic stability and epigenesis in randomly constructed genetic nets. *J Theor Biol* 22:437–467.
- Li F, Long T, Lu Y, Ouyang Q, Tang C (2004) The yeast cell-cycle network is robustly designed. *Proc Natl Acad Sci USA* 101:4781–4786.
- Huang S, Eichler G, Bar-Yam Y, Ingber DE (2005) Cell fates as high-dimensional attractor states of a complex gene regulatory network. *Phys Rev Lett* 94:128701.
- Huang S, Guo YP, May G, Enver T (2007) Bifurcation dynamics in lineage-commitment in bipotent progenitor cells. *Dev Biol* 305:695–713.
- Wang J, Xu L, Wang E, Huang S (2010) The potential landscape of genetic circuits imposes the arrow of time in stem cell differentiation. *Biophys J* 99:29–39.
- Wang J, Zhang K, Xu L, Wang E (2011) Quantifying the Waddington landscape and biological paths for development and differentiation. *Proc Natl Acad Sci USA* 108:8257–8262.
- Huang S (2012) The molecular and mathematical basis of Waddington's epigenetic landscape: A framework for post-Darwinian biology? *Bioessays* 34:149–157.
- Li C, Wang J (2013) Quantifying Waddington landscapes and paths of non-adiabatic cell fate decisions for differentiation, reprogramming and transdifferentiation. *J R Soc Interface* 10:20130787.
- Scialdone A, et al. (2016) Resolving early mesoderm diversification through single-cell expression profiling. *Nature* 535:289–293.
- Bargajé R, et al. (2017) Cell population structure prior to bifurcation predicts efficiency of directed differentiation in human induced pluripotent cells. *Proc Natl Acad Sci USA* 114:2271–2276.
- Jolly MK, et al. (2014) Towards elucidating the connection between epithelial-mesenchymal transitions and stemness. *J R Soc Interface* 11:20140962.
- Steinway SN, et al. (2014) Network modeling of TGF-beta signaling in hepatocellular carcinoma epithelial-to-mesenchymal transition reveals joint sonic hedgehog and wnt pathway activation. *Cancer Res* 74:5963–5977.
- Steinway SN, et al. (2015) Combinatorial interventions inhibit TGF $\beta$ -driven epithelial-to-mesenchymal transition and support hybrid cellular phenotypes. *NPJ Syst Biol Appl* 1:15014.
- Huang B, et al. (2017) Interrogating the topological robustness of gene regulatory circuits by randomization. *PLoS Comput Biol* 13:e1005456.
- Sethna JP, et al. (1993) Hysteresis and hierarchies: Dynamics of disorder-driven first-order phase transformations. *Phys Rev Lett* 70:3347–3350.
- Pázmándi F, Zaránd G, Zimányi GT (1999) Self-organized criticality in the hysteresis of the Sherrington-Kirkpatrick model. *Phys Rev Lett* 83:1034–1037.
- Samavarchi-Tehrani P, et al. (2010) Functional genomics reveals a BMP-driven mesenchymal-to-epithelial transition in the initiation of somatic cell reprogramming. *Cell Stem Cell* 7:64–77.
- Li R, et al. (2010) A mesenchymal-to-epithelial transition initiates and is required for the nuclear reprogramming of mouse fibroblasts. *Cell Stem Cell* 7:51–63.
- Bornholdt S (2008) Boolean network models of cellular regulation: Prospects and limitations. *J R Soc Interface* 5(Suppl 1):S85–S94.
- Derrida B (1987) Dynamical phase transition in nonsymmetric spin glasses. *J Phys A Math Gen* 20:L721–L725.
- Gutfreund H, Reger JD, Young AP (1988) The nature of attractors in an asymmetric spin glass with deterministic dynamics. *J Phys A Math Gen* 21:2775–2797.
- Mezard M, Parisi G, Virasoro MA (1987) *Spin Glass Theory and Beyond* (World Scientific, Singapore).
- Hed G, Hartmann AK, Stauffer D, Domany E (2001) Spin domains generate hierarchical ground state structure in  $J = +/-1$  spin glasses. *Phys Rev Lett* 86:3148–3151.
- Hed G, Young AP, Domany E (2004) Lack of ultrametricity in the low-temperature phase of three-dimensional Ising spin glasses. *Phys Rev Lett* 92:157201.
- Derrida B, Flyvbjerg H (1986) Multivalley structure in Kauffman's model: Analogy with spin glasses. *J Phys A Math Gen* 19:L1003–L1008.
- Miranda EN, Parga N (1988) Ultrametricity in the Kauffman model: A numerical test. *J Phys A Math Gen* 21:L357–L361.
- Bastolla U, Parisi G (1996) Closing probabilities in the Kauffman model: An annealed computation. *Physica D Nonlinear Phenomena* 98:1–25.
- Carithers LJ, et al. (2015) A novel approach to high-quality postmortem tissue procurement: The GTEx project. *Biopreservation and Biobanking* 13:311–319.
- Abnaof K, et al. (2014) Tgf-beta stimulation in human and murine cells reveals commonly affected biological processes and pathways at transcription level. *BMC Syst Biol* 8:55.
- Chu LF, et al. (2016) Single-cell RNA-seq reveals novel regulators of human embryonic stem cell differentiation to definitive endoderm. *Genome Biol* 17:173.
- Liu Z, et al. (2017) Single-cell transcriptomics reconstructs fate conversion from fibroblast to cardiomyocyte. *Nature* 551:100–104.
- Puram SV, et al. (2017) Single-cell transcriptomic analysis of primary and metastatic tumor ecosystems in head and neck cancer. *Cell* 171:1611–1624.e24.